



UNIVERSITY OF LEEDS

This is a repository copy of *Enhanced magnetic coercivity of α -FeO obtained from carbonated 2-line ferrihydrite*.

White Rose Research Online URL for this paper:
<http://eprints.whiterose.ac.uk/78765/>

Version: Accepted Version

Article:

Vallina, B, Rodriguez-Blanco, JD, Benning, LG et al. (2 more authors) (2014) Enhanced magnetic coercivity of α -FeO obtained from carbonated 2-line ferrihydrite. *Journal of Nanoparticle Research*, 16 (3). 2322. ISSN 1388-0764

<https://doi.org/10.1007/s11051-014-2322-5>

Reuse

Unless indicated otherwise, fulltext items are protected by copyright with all rights reserved. The copyright exception in section 29 of the Copyright, Designs and Patents Act 1988 allows the making of a single copy solely for the purpose of non-commercial research or private study within the limits of fair dealing. The publisher or other rights-holder may allow further reproduction and re-use of this version - refer to the White Rose Research Online record for this item. Where records identify the publisher as the copyright holder, users can verify any specific terms of use on the publisher's website.

Takedown

If you consider content in White Rose Research Online to be in breach of UK law, please notify us by emailing eprints@whiterose.ac.uk including the URL of the record and the reason for the withdrawal request.



eprints@whiterose.ac.uk
<https://eprints.whiterose.ac.uk/>

promoting access to White Rose research papers



Universities of Leeds, Sheffield and York
<http://eprints.whiterose.ac.uk/>

This is an author produced version of a paper published in **Journal of Nanoparticle Research**

White Rose Research Online URL for this paper:

<http://eprints.whiterose.ac.uk/id/eprint/78765>

Paper:

Vallina, B, Rodriguez-Blanco, JD, Benning, LG, Blanco, JA and Brown, AP (2014) *Enhanced magnetic coercivity of α -FeO obtained from carbonated 2-line ferrihydrite*. Journal of Nanoparticle Research, 16 (3). 2322. ISSN 1388-0764

<http://dx.doi.org/10.1007/s11051-014-2322-5>

34 the subparticle structure induced by the different particle and crystallite size growth
35 rates at increasing annealing temperature.

36

37 **1. INTRODUCTION**

38 Iron oxides are very widespread in nature and they have attracted considerable
39 attention in various scientific disciplines particularly due to the unique combination of
40 electronic, chemical, optical, and thermal properties (Cornell and Schwertmann
41 2003). Among the sixteen known iron oxy(hydro)xides (Cornell and Schwertmann
42 2003), α -Fe₂O₃ (hematite) is considered the ideal candidate for many technological
43 applications due to its low cost, biodegradability, high resistance to corrosion and
44 high stability (e.g.: Gubin et al. 2005; Zhu et al. 2011; Jacob et al. 2010). Over the last
45 decade, research efforts were focused on the development of α -Fe₂O₃-bearing
46 materials with potential technological applications in catalysis (Fang et al. 2009),
47 hydrocarbon and carbon monoxide gas sensors (e.g., Cornell and Schwertmann 2003),
48 pigments (e.g., Ni et al. 2009), water treatment (e.g., Guo et al. 2011), rechargeable
49 batteries (Pan et al. 2009), adsorbents (Muruganandham et al. 2011), biomedicine
50 (e.g., Liu et al. 2011), semiconductors (e.g., Bahgat et al. 2006), or optical and
51 electromagnetic devices (e.g., Tsuzuki et al. 2011). Despite this plethora of research,
52 some of the magnetic properties of synthetic α -Fe₂O₃ are still not fully understood
53 (Lovesey et al. 2011; Tadic et al. 2012).

54 α -Fe₂O₃ is weakly ferromagnetic at ambient temperature with a Neel
55 temperature of \sim 953 K (Xu et al. 2009). However, α -Fe₂O₃ changes from weakly
56 ferromagnetic to antiferromagnetic below room temperature, a magnetic phase
57 transition known as the Morin transition (Cornell and Schwertmann 2003). This
58 Morin transition temperature decreases with particle size and it is completely
59 suppressed when the α -Fe₂O₃ particles become smaller than \sim 20 nm (Tadic et al.
60 2011; Tadic et al. 2012; Bercoff and Bertorello 2010). Similarly to the Morin
61 transition temperature, other magnetic properties of α -Fe₂O₃ can dramatically change
62 with particle or Scherrer crystallite size, particle morphology, interparticle
63 interactions, synthesis pressure, or with doping (Jacob et al. 2010; Sahu et al. 1997;
64 Suber et al. 2010; Chuanbo et al., 2010). For example, depending on the preparation
65 method (e.g., hydrothermal synthesis vs. mechanical grinding), particle morphology
66 or particle microstructure can lead to magnetic coercivities for α -Fe₂O₃ as high as a

67 few kOe (e.g.: Rat et al. 1999; Yang et al. 2011). Most studies suggest that the
68 presence of a subparticle structure in the α -Fe₂O₃ nanocrystals may explain such high
69 coercivities. However, this is still a matter of debate, as the correlation between
70 morphology, microstructure, particle interactions and magnetic properties of α -Fe₂O₃
71 are still ambiguous and the exact reasons for this behavior are not fully understood.

72 The next needed development is the design and testing of novel methods for
73 controlled synthesis of α -Fe₂O₃ nanocrystals with specific chemical, physical and
74 magnetic properties that can be exploited for potential technological applications.
75 Most studies that addressed the synthesis of α -Fe₂O₃ employed a solvothermal
76 approach (An et al. 2012; Mitra et al. 2007; Xu et al. 2012; Wang et al. 2011; Zhang
77 and Chen 2009) or hydrothermal methods (e.g.: Tadić et al. 2011; Song et al. 2009;
78 Song et al. 2011; Li et al. 2007; Ni et al. 2012; Li et al. 2009; Peng et al. 2010;
79 Davidson et al 2008; Vu et al. 2010; Zhu et al. 2006; Zhong et al. 2008; Zhang et al.
80 2008; Jia et al. 2012; Lu et al. 2008; Islam et al. 2012; Jia et al. 2011; Suresh et al.
81 2013 and references therein). In recent years, producing α -Fe₂O₃ via dry thermal
82 treatments of iron-bearing precursor phases has become a common synthesis method.
83 An iron oxyhydroxide precursor phase that is very common in both natural
84 environments and laboratory synthesis studies is the poorly-ordered phase
85 ferrihydrite. Its precise chemical formula and structure are the subject of much recent
86 debate (Cornell and Schwertmann 2003; Yu et al. 2002; Brequo et al. 2007; Liu et al.
87 2009; Michel et al. 2010) in part because ferrihydrite is the crucial precursor for α -
88 Fe₂O₃ – the mineral hematite. This poorly-crystalline phase is usually termed 2-line or
89 6-line ferrihydrite according to the number of broad Bragg peaks observed in its
90 powder X-ray diffraction pattern (Cornell and Schwertmann 2003). To synthesize
91 ferrihydrite in the laboratory three different methods are usually employed: *a*)
92 neutralizing a ferric salt solution (e.g.: Stanjek and Weidler 1992; Zhao et al. 1994;
93 Carta et al. 2009; Xu et al. 2011), *b*) dialyzing a ferric nitrate solution (e.g., Cornell
94 and Schwertmann 2003;) or *c*) oxidizing a ferrous salt solution (Schwertmann and
95 Taylor 1972). Once 2- or 6-line ferrihydrite is synthesized it is crystallized to α -Fe₂O₃
96 either by dry heating (Stanjek and Weidler 1992; Schneeweiss et al. 2008), through
97 hydrothermal routes (e.g., Vu et al. 2010; Xu et al. 2011) or through slow aging in
98 solution (Raiswell et al. 2010). However, most of these studies had the primary goal

99 to only characterize the ferrihydrite structure or stability and not the properties of the
100 final product, α -Fe₂O₃.

101 In this current study therefore, we took a two-step approach. We designed and
102 tested a novel method that allowed us to produce α -Fe₂O₃ with high magnetic
103 coercivities from a precursor 2-line ferrihydrite, yet this precursor was itself produced
104 via a novel green-chemical method in the presence of carbonate. This carbonated 2-
105 line ferrihydrite precursor was formed following an equivalent methodology to an
106 often employed approach used for the production of amorphous carbonate or
107 phosphate precursors (Rodriguez-Blanco et al. 2008; Vallina et al. 2013; Roncal-
108 Herrero et al. 2009). After synthesis the resulting solids were dry-heated from 350 to
109 1000 °C and the crystalline product, α -Fe₂O₃, was characterized with X-ray
110 diffraction, high-resolution microscopy and magnetometry. A correlation between the
111 magnetic properties of this novel α -Fe₂O₃ and its structure at the nanoscale is reported
112 and discussed.

113

114 **2. EXPERIMENTAL**

115 The synthesis of α -Fe₂O₃ was performed in two steps: firstly, an aqueous
116 solution containing 50 mM of Fe(NO₃)₃·9H₂O (Sigma-Aldrich, 99.9% purity) was
117 added to an aqueous solution containing 50 mM of Na₂CO₃ (Fisher Scientific, 99.9%
118 purity) at ambient temperature. The mixed solutions were rapidly filtered under
119 vacuum through 0.2 μm polycarbonate membranes, obtaining a dark reddish
120 precipitate. This solid was immediately washed with Milli-Q water and isopropanol
121 and dried at room temperature, following Rodriguez-Blanco et al. (2008). The so
122 obtained dry solids were dry-heated to specific temperatures (350, 600, 800 and 1000
123 °C) following a 3-hour thermal equilibration and then allowed to cool down to room
124 temperature.

125 The initial precipitate and the temperature-dependent crystalline end products
126 were identified by powder X-ray diffraction (XRD) using a Panalytical X'Pert Pro
127 diffractometer (CuK α _{1,2}; 2 θ range 20-70; 0.01°/step and 0.3 s/step). In order to also
128 follow the crystallization of the initial precursor phase to α -Fe₂O₃, and to identify any
129 potential intermediate phase transformations during the heating process, we also
130 employed the same diffractometer with an additional Anton Paar HTK 1200N High-
131 Temperature Oven-Chamber, and carried out powder X-ray thermodiffraction.

132 Thermodiffraction patterns were collected from 25 to 1000 °C (at a constant heating
133 ramp of 1 °C/min.; 2θ range 20-50 at 0.01°/step and 0.16 s/step) while running the
134 system at atmospheric conditions. Pattern-matching refinement of the crystalline
135 phases was carried out using the Rietveld refinement software TOPAS (Coelho,
136 2003). Crystallite sizes were estimated from the diffraction patterns using the Scherrer
137 equation (Scherrer, 1918), with the assumption that the particles were stress-free and
138 taking into account the X-ray pattern of a LaB₆ standard (ICDD PDF 34-0427; $2\theta_{110}$ =
139 30.36° and FWHM= 0.06°). The precursor phase was also analyzed with Fourier
140 transform infrared (FTIR) spectroscopy, thermogravimetric analyses (TGA) and
141 transmission electron microscopy (TEM). FTIR spectra were acquired on an A2-
142 Technology Microlab Portable mid-IR spectrometer with a Diamond internal
143 reflection cell (DATR). FTIR spectra were collected by co-adding 1024 scans in the
144 650-4000 cm⁻¹ range at a resolution of 4 cm⁻¹. The Thermo Nicolet OMNIC ESP 5.1
145 software package was used to manipulate the spectra, including baseline subtraction.
146 Thermo gravimetric analyses were carried out with a Mettler TA 4000 instrument,
147 while heating the samples from 25 to 1000 °C at a rate of 10 °C/min in a nitrogen
148 atmosphere. Finally, using a field emission gun transmission electron microscope
149 (FEG-TEM; FEI CM200; operated at 197 kV and equipped with an Oxford
150 Instruments energy-dispersive X-ray (EDX) analysis system (Isis) and a Gatan
151 Imaging Filter (GIF-200) the precursor phase was imaged and spectrally analysed.

152 Complementing the data set of the precursor phase, we also imaged and
153 analyzed the morphology and structural characteristics of the crystalline end product
154 phases using a FEG scanning electron microscope (FEG-SEM, LEO 1530 Gemini,
155 operated at 3 kV and with an in-lens detector, equipped with an energy-dispersive X-
156 ray (EDX) analysis system; Isis) and a high-resolution TEM (HR-TEM; MET JEOL-
157 JEM 2100F, with an in-lens detector, equipped with an energy-dispersive X-ray
158 (EDX) analysis system). Finally, the temperature-dependent crystalline end products
159 were fully characterized for their magnetic properties at room temperature using a
160 vibrating sample magnetometer (EV9 VSM) with a maximum magnetic field of 20
161 kOe. Magnetic hysteresis measurements were conducted in an applied magnetic field
162 sweeping from -20 to 20 kOe.

163

164 3. RESULTS AND DISCUSSION

165 3.1. Characterization of carbonate bearing-ferrihydrite

166 High-resolution TEM images of the dark reddish precipitate that formed
167 immediately upon mixing of the starting solutions revealed that it consisted of
168 agglomerates of nanoparticles (< 20 nm in size) of amorphous to nanocrystalline
169 character (Fig 1). Standarless quantification of EDX spectra indicated a ~ 24 % C, ~
170 34 % O and ~ 38% Fe content (Fig 1a, inset) and Electron Energy Loss Spectroscopy
171 (EELS) suggested some carbonate (from the sharp peak at ~ 290 eV at the C K-edge)
172 plus a ferrihydrite structure (O K-edge) that was predominately ferric (Fe L-edge),
173 with amorphous or disordered carbon adsorbed or co-precipitated (Fig. SI-1). Selected
174 area electron diffraction (SAED) patterns showed two broad, diffuse rings at ~ 1.5
175 and ~ 2.5 Å consistent with a 2-line ferrihydrite pattern (Cornell and Schwertmann
176 2003). High magnification images also revealed small particles with diffuse lattice
177 fringes (Fig 1b).

178 Powder X-ray diffraction of this initial amorphous material (Fig. 2) showed two
179 broad humps centered at approximately 35° and 63° 2θ, consistent with the amorphous
180 to nanocrystalline nature of the carbon containing 2-line ferrihydrite identified by
181 TEM. The FTIR spectrum of this 2-line ferrihydrite (Table 1; Fig. 2, inset) was
182 characterized by the broad and prominent band in the range ~ 3700 and 2300 cm⁻¹ and
183 the band at ~ 1633 cm⁻¹, which were ascribed to the stretching and bending of OH
184 groups, respectively. These bands were attributed to adsorbed or structural water (Liu
185 et al. 2009; Farmer, 1974). The bands at ~ 1385 and 1338 cm⁻¹ were assigned to Fe-
186 OH vibrations. The spectrum also showed a weak band at 824 cm⁻¹, which was
187 attributed to the bending vibration of hydroxyl groups of iron hydroxides (Fe-OH)
188 (Rout et al. 2012). Interestingly, the FTIR spectra revealed the presence of carbonate
189 bonds in association with the 2-line ferrihydrite precursor. This is evidenced in the
190 weak bands at ~ 1455 and ~ 1042 cm⁻¹, which are typical of the stretching vibrations
191 of the carbonate ion (Farmer, 1974). Such carbonate bands are often observed in
192 ferrihydrite FTIR spectra because of its susceptibility to CO₂ adsorption from air (Liu
193 et al. 2009). However, in our case, the high percentage of C detected by TEM – EELS
194 (Fig. SI-1) suggests that the carbonate adsorbed or co-precipitated with our 2-line
195 ferrihydrite. Thus our FTIR spectra did not just reveal atmospheric CO₂ adsorption,
196 but indicates carbonate that is closely associated with the 2-line ferrihydrite and thus

197 we suppose the carbonate seen in the spectra must have been derived from the
198 Na_2CO_3 reagent used in our synthesis.

199 The TGA data of the 2-line ferrihydrite (Fig. 3) showed that upon heating a total
200 weight loss of approximately $\sim 35\%$ occurred of which $\sim 10\%$ was lost below $100\text{ }^\circ\text{C}$
201 and the other $\sim 25\%$ was lost between 100 and $480\text{ }^\circ\text{C}$, after which no more changes
202 were observed. Although little is known about the dehydration of 2-line ferrihydrite,
203 the weight loss of our solid during the TGA analyses was slightly higher than values
204 ($23\text{-}25\%$) reported by other authors (Carta et al. 2009; Xu et al. 2011; Eggleton et al.
205 1988). The high water content in our 2-line ferrihydrite that was confirmed by our
206 FTIR data (Fig. 2, inset) indicates a weight loss with increasing temperature
207 consistent with dehydration (Cornell and Schwertmann 2003, Carta et al. 2009;
208 Eggleton et al. 1988). However, both HR-TEM and FTIR data clearly indicated a
209 carbonate association with the 2-line ferrihydrite (Fig 1, 2 inset and Fig. S1). Thus we
210 hypothesise that part of the weight loss must be a consequence of the decomposition
211 of CO_3 to CO_2 . This carbonate loss is predicted to occur above $300\text{ }^\circ\text{C}$ (Galwey and
212 Brown 1999) and can be seen to happen in our samples at $\sim 480\text{ }^\circ\text{C}$ (Fig, 3 first
213 derivative curve).

214 Taken as a whole, the XRD, HR-TEM, FTIR and TGA data point towards a
215 new compound that we label, carbonated 2-line ferrihydrite, consistent with a
216 previous report (Liu et al. 2008). It has to be noted however, that the structure and
217 precise composition of our carbonated 2-line ferrihydrite is unknown. Indeed the
218 structures and formulas of all ferrihydrites are still the subject of intense debate
219 (Cornell and Schwertmann 2003; Yu et al. 2002; Berquó et al. 2007; Liu et al. 2009;
220 Michel et al. 2010) and so far no definitive consensus has been reached. Obtaining the
221 exact formula or structural characteristics of our new, carbonate-rich 2-line
222 ferrihydrite is outside the scope of this study.

223

224 **3.2. Hematite properties synthesized from carbonated 2-line ferrihydrite**

225 Our carbonated 2-line ferrihydrite was dry-heated from 25 to $1000\text{ }^\circ\text{C}$, with
226 simultaneous recording of thermodiffraction patterns (Fig. 4). Initially the XRD
227 patterns exhibited only a large background hump (at $\sim 35\text{ }2\theta$) with no distinct
228 diffraction peaks and no detectable change upon heating up to $250\text{ }^\circ\text{C}$. Only at
229 higher temperatures did small Bragg peaks at 33.15° and $35.61^\circ\text{ }2\theta$ start to develop

230 concomitantly with a decrease in the background intensity. These new peaks
231 correspond to the most intense Bragg peaks of α -Fe₂O₃ (hematite; ICDD PDF 33-
232 0664, $a = 5.03 \text{ \AA}$, $c = 13.74 \text{ \AA}$). Once the crystallization of α -Fe₂O₃ was initiated, the
233 only observed changes with temperature were a reduction in width and an increase in
234 intensity of the α -Fe₂O₃ peaks up to $\sim 500 \text{ }^\circ\text{C}$. From 500 to 1000 $^\circ\text{C}$ the intensity of
235 the Bragg peaks remained constant, but they became narrower as the temperature
236 increased. No other crystalline solids were observed during the reaction. The
237 refinement of the X-ray diffraction patterns of samples obtained at 350, 600, 800 and
238 1000 $^\circ\text{C}$ (Fig. 5) confirmed they are all consistent with only α -Fe₂O₃. An evaluation
239 of the Scherrer crystallite size showed a linear increase of the crystallite size with
240 temperature from 20 nm at 350 $^\circ\text{C}$ to 131 nm at 1000 $^\circ\text{C}$ (Table 2; Fig. SI-2). High-
241 resolution microscopy revealed the morphologies of the α -Fe₂O₃ samples, as well as
242 the particle sizes and internal structures (Fig. 6 and 7). At 350 $^\circ\text{C}$ (Fig. 6a and 7a) and
243 600 $^\circ\text{C}$ (Fig. 6b and 7c) the particles have a pseudospheric morphology, but at 800 $^\circ\text{C}$
244 (Fig. 6c) and 1000 $^\circ\text{C}$ (Fig. 6d) they are prismatic. The average particle dimensions
245 were evaluated by measuring the width (W) and length (L) of 100 particles in each
246 sample (Fig. SI-3). The particle sizes increased from $20 \pm 6 \text{ (L)} \times 15 \pm 4 \text{ (W)} \text{ nm}$ at 350
247 $^\circ\text{C}$ to $352 \pm 119 \text{ (L)} \times 277 \pm 103 \text{ (W)} \text{ nm}$ at 1000 $^\circ\text{C}$ (Table 2). HR-TEM images of α -
248 Fe₂O₃ confirmed that the particles were crystalline with interplanar spacings of ~ 3.7 ,
249 2.7, 2.2 and 1.7 \AA visible (Fig. 7), which correspond to the (012), (104), (113) and
250 (116) d-spacings of α -Fe₂O₃. The SAED patterns (insets in Fig 7) corroborate the
251 temperature-dependent increase in Scherrer crystallite size (Figs. 4, 5 and Table 2).
252 The SAED pattern of the sample produced at 350 $^\circ\text{C}$ (Fig. 7b, inset) showed diffuse
253 diffraction rings with poorly developed spots, evidencing the presence of very small,
254 nanocrystalline particles. In contrast, only discrete spots were observed in samples
255 produced at higher temperatures (e.g., Fig. 7h, inset). The HR-TEM images also
256 revealed temperature-dependent structural differences at the nanoscale: at 350 $^\circ\text{C}$ the
257 average particle size was of $20 \times 15 \text{ nm}$ (Fig. 7 a, b), matching the Scherrer crystallite
258 sizes. At 600 $^\circ\text{C}$ the average particle size was $\sim 71 \times 52 \text{ nm}$ (Fig. 7c, d), which is
259 slightly larger than the Scherrer crystallite size ($\sim 55 \text{ nm}$). However, the sizes of the
260 prismatic particles obtained at 800 and 1000 $^\circ\text{C}$ (Fig. 6 c,d; Fig. 7 e, g) were much
261 larger (202×136 and $352 \times 277 \text{ nm}$, respectively) than their Scherrer crystallite sizes
262 (92 and 131 nm, respectively). This revealed that a significant number of the

263 prismatic particles were made of nanocrystalline subparticles of various sizes down to
264 ~20 nm (e.g.: Fig. 7 i, j). These data indicates that α -Fe₂O₃ synthesized from
265 carbonated 2-line ferrihydrite at lower temperatures (350-600 °C) grows as single
266 nanocrystals. In contrast, at higher temperatures (800-1000 °C) the formed α -Fe₂O₃
267 particles consist of aggregates of nanocrystalline subparticles (Rath et al. 1999).

268 The magnetic measurements of various crystalline end product α -Fe₂O₃ also
269 revealed a synthesis temperature-dependent behavior (Fig. 8, Table 2). The α -Fe₂O₃
270 sample obtained at 350 °C exhibited a very small hysteresis loop with a remanent
271 magnetization (Mr) of 0.007(1) emu/g and coercivity (Hc) of only ~ 289 Oe.
272 Conversely, the hysteresis loop of the sample crystallized at 600 °C showed a weak
273 ferromagnetic behaviour with a remanent magnetization of 0.032(5) emu/g but a
274 higher magnetic coercivity of ~ 1720 Oe while at 800 °C and 1000 °C very wide-open
275 hysteresis loops, indicating a stronger ferromagnetic behaviour with remanent
276 magnetization and coercivity values of 0.011(4) emu/g and ~ 3837 Oe (800 °C) and
277 0.025(5) emu/g and ~ 5027 Oe (1000 °C), respectively were observed. Note however,
278 that the hysteresis loops did not reach magnetization saturation, even at the maximum
279 applied magnetic field. Nonetheless these data clearly indicate a drastic change in
280 magnetic properties with increasing crystallization temperature.

281 The understanding of this temperature-dependent magnetic behavior requires
282 comparison with the nanoscale structural characteristics of the α -Fe₂O₃. Fig. 9 shows
283 the variation of magnetic coercivity with particle size, Scherrer crystallite size and
284 temperature. There is a linear proportionality between coercivity and Scherrer
285 crystallite size and between coercivity, magnetization energy density and temperature,
286 but the relationship between the coercivity and particle size follows a logarithmic
287 trend. Although our results regarding these trends are in agreement with several
288 studies (Rath et al. 1999; Bercoff and Bertorello 2010; Sahu et al. 1997; Bao et al.
289 2011), the dependence between magnetic coercivity, temperature and particle size is
290 still a matter of debate. Using different synthesis methods various other authors have
291 reported decreasing coercivity values with increasing particle sizes (Jacob and Khadar
292 2010; Kletetschka and Wasilewski 2002; Li et al. 2002; Yao and Cao 2012). This has
293 also been observed in natural α -Fe₂O₃, with a very gradual decrease in coercivity at
294 sizes above 100 μ m (Kletetschka and Wasilewski 2002). Interestingly, the effect of
295 thermally-induced growth on the coercivity field and magnetization energy density

296 has been addressed for Ni thin films. Kumar et al (2009) and Kumar (2010) reported
297 that the magnetic behaviour of Ni thin films was dependent on grain size, in particular
298 on the width of the grain boundary walls. By using atomic force microscopy they
299 revealed that the thermally-induced increase of the grain size produced a densification
300 of the solid which was translated into a decrease of the width of the grain boundaries.
301 This transition from a nanocrystalline to crystalline structure caused a maximum in
302 the coercive field, which then decreased with increase of particle size, similarly to
303 other Fe- or Co-bearing alloys and compounds (Cullity and Graham, 2008). Our high-
304 resolution microscopy images of α -Fe₂O₃ (Fig. 6 and 7) revealed a progressive
305 decrease of the width of the grain boundary sizes with temperature. Also the
306 dependence of the magnetic coercivity on the particle size of α -Fe₂O₃ followed a
307 logarithmic trend (Fig. 9), so we hypothesize that the maximum of the coercivity field
308 in our system was not reached. This maximum and a subsequent decrease of the
309 magnetic coercivity may occur at temperatures above 1000 °C and after longer
310 annealing times.

311 However, compared to our dry-heating experiments, most of the research for
312 α -Fe₂O₃ has been carried out on synthetic hematite obtained under hydrothermal
313 conditions. For example, hematite nanodiscs ($\phi = 78 - 150$ nm) obtained
314 hydrothermally from FeCl₃, NaH₂PO₄ and ethanol glycol at 200 °C reached coercivity
315 values between 22 and 214 Oe. Hydrothermal synthesis (70-180 °C) of α -Fe₂O₃ using
316 ferrihydrite as a precursor resulted in coercivity values between 670 and 2600 Oe
317 after reaction times between 2 hours and 44 days (Liu et al. 2010). Some researchers
318 explain these magnetic properties as a consequence of magnetocrystalline and/or
319 magnetoelastic anisotropies. However, in the literature there is plethora of research
320 about the synthesis of α -Fe₂O₃ with many different morphologies whose coercivity
321 values are explained by shape anisotropy (e.g.: An et al. 2012; Pan et al. 2009;
322 Muruganandham et al. 2011; Liu et al. 2011; Rath et al. 1999; Tsuzuki et al. 2011;
323 Tadic et al. 2012; Xu et al. 2009; Bercoff and Bertorello 2012; Suber et al. 2010;
324 Chang et al. 2010; Xu et al. 2013; Zhang et al. 2013). Anisotropic particle
325 morphologies induce high magnetic coercivities because the magnetic spins are
326 preferentially aligned along the easy magnetic axes and their reversals to other
327 directions require more energy in comparison with spherical or pseudospherical
328 particles (An et al. 2012; Pan et al. 2009; Tadic et al. 2012; Mitra et al. 2007; Zeng et

329 al. 2007). In our experiments the morphology of the α -Fe₂O₃ changed from
330 pseudospherical to prismatic with increasing temperature. However, the length/width
331 ratio of our particles was very similar (~1.3) throughout, showing no significant
332 variations across the whole temperature range between 350 and 1000 °C. We cannot
333 discard a contribution of shape anisotropy to the coercivity of our α -Fe₂O₃ however,
334 we consider that in our experiments the effect of temperature on the shape anisotropy
335 is very small or negligible.

336 Nevertheless, in our experiments, temperature played an important role on
337 controlling the particle and Scherrer crystallite size growth (Fig. SI-2). Considering
338 that the crystallization of α -Fe₂O₃ started at ~ 250 °C (Fig. 4) and the rate of heating
339 for all the samples was the same (1 °C/minute), our data (Table 2; Fig. SI-2) indicate
340 that the growth of the Scherrer crystallite sizes with temperature took place at a
341 slower rate (~0.17 nm/°C) than the growth of the particle sizes (~0.43 nm/°C). These
342 different growth rates are translated into a progressive, temperature-dependent,
343 development of a subparticle structure, i.e. from single-nanocrystals at 350 °C to
344 aggregates of nanocrystalline subparticles at 1000 °C (Fig. 7). Our HR-TEM images
345 also suggest that the subparticles observed at 800-1000 °C (Fig. 7 i, j) were relicts of
346 the single-nanocrystals observed at 350 °C (Fig. 7 a, b), and this is a result of the
347 intergrowth and aggregation of these single-nanocrystals during the dry-heating
348 process. It is thus also not surprising that the growth of these aggregates with a
349 subparticle-structure permits stronger magnetic interactions: the unusual high
350 coercivity reached at 800-1000 °C is most likely a consequence of the contribution of
351 the individual subparticles as well as the contribution from the interactions between
352 these particles (Rath et al. 1999; Tadic et al. 2012). At lower temperature this
353 subparticle structure is completely absent and therefore the low coercivity values are
354 only a consequence of the contribution of the single nanocrystals.

355

356 **4. CONCLUSIONS**

357 This study demonstrates that enhanced magnetic coercivities for α -Fe₂O₃ can be
358 achieved using a facile method, consisting of dry-heating a carbonated 2-line
359 ferrihydrite precursor prepared from solution. α -Fe₂O₃ exhibited temperature-
360 dependent magnetic coercivity values ranging from 289 to 5027 Oe. The origin of
361 these high coercivity values is interpreted as being a consequence of the slower

362 growth rate of the Scherrer crystallite size with respect to the particle size during the
363 heating process. These differences in the growth rates are also translated into a
364 progressive development of a subparticle structure at the nanoscale. At lower
365 temperatures (350-600 °C) single particles crystallize however, at higher temperatures
366 (> 600 °C) the growth of crystalline aggregates with a subparticle-structure is
367 favoured.

368

369 **5. ACKNOWLEDGEMENTS**

370 This research was supported by the Spanish Ministry of Economy and
371 Competitivity (MICINN-12-MAT2011-27573-C04-02) and the Marie Curie EU-
372 FP6 MINGRO Research and Training Network under contract MRTNCT-2006-
373 035488. The authors would like to thank the Cohen Laboratories at the School of
374 Earth and Environment and the Leeds Electron Microscopy and Spectroscopy
375 Centre (LEMAS) at the Faculty of Engineering (University of Leeds). The help of
376 David Martínez Blanco (Scientific-Technical Services of the University of Oviedo,
377 Spain) with the magnetic measurements is also acknowledged.

378

379 **6. REFERENCES**

380

381 Al-Gaashani R, Radiman S, Tabet N, Daud AR (2013) Rapid synthesis and optical
382 properties of hematite (α -Fe₂O₃) nanostructures using a simple thermal decomposition
383 method. *J Alloy Compd* 550:395-401. Doi: 10.1016/j.jallcom.2012.10.150

384

385 An Z, Zhang J, Pan S, Song G (2012) Novel peanut-like α -Fe₂O₃ superstructures:
386 Oriented aggregation and Ostwald ripening in a one-pot solvothermal process.
387 *Powder Technol* 217:274-280. doi: 10.1016/j.powtec.2011.10.038

388

389 Andersen FA, Brečević L (1991) Infrared Spectra of Amorphous and Crystalline
390 Calcium Carbonate. *Acta Chem Scand* 45:1018-1024. doi: 10.1002/chin.199209005

391

392 Bahgat M, Khedr MH, Nasr MI, Sedeek EK (2006) Effect of temperature on
393 reduction of nanocrystalline Fe₂O₃ into metallic iron. *Mater Sci Tech Ser* 22:315-320.
394 doi: 10.1179/026708306X81559

395

396 Bao L, Yang H, Wang X, Zhang F, Shi R, Liu B, Wang L, Zhao H (2011) Effect of
397 temperature on reduction of nanocrystalline Fe₂O₃ into metallic iron. *J Cryst Growth*
398 328:62-69. doi: 10.1016/j.jcrysgro.2011.05.030

399

400 Bercoff PG, Bertorello HR (2010) Magnetic properties of hematite with large
401 coercivity. *App. Phys. A-Mater* 100:1019-1027. doi: 10.1007/s00339-010-5983-7

402

403 Berquó TS, Banerjee SK, Ford RG, Penn RL, Pichler T (2007) High Crystallinity Si-
404 Ferrihydrite: An Insight Into Its Neel Temperature and Size Dependence of Magnetic
405 Properties. *J Geophys Res* 112:B02102. doi: 10.1029/2006JB004583
406
407 Carta D, Casula MF, Corrias A, Falqui A, Navarra G, Pinna G (2009) Structural and
408 magnetic characterization of synthetic ferrihydrite nanoparticles *Mater Chem Phys*
409 113:349-355. doi: 10.1016/j.matchemphys.2008.07.122
410
411 Chang C, Zhang C, Wang W, Li Q (2010) Preparation and magnetic properties of
412 Fe₂O₃ microtubules prepared by sol-gel template method. *Rare Metals* 29:501-504.
413 doi: 10.1007/s12598-010-0156-6
414
415 Coelho AA (2003) TOPAS: General Profile and Structure Analysis Software for
416 Powder Diffraction Data.
417
418 Cornell RM, Schwertmann U (2003) The iron oxides: structure, properties, reactions
419 and occurrences and uses. Wiley-VCH, Weinheim.
420
421 Cullity B D, Graham C D (2008) Introduction to Magnetic Materials. Wiley-IEEE
422 Press. Piscataway, NJ.
423
424 Davidson LE, Shaw S, Benning LG (2008) The kinetics and mechanisms of
425 schwertmannite transformation to goethite and hematite under alkaline conditions.
426 *Am Mineral* 93:1326-1337. doi:10.2138/am.2008.276
427
428 Diaz-Guerra C, Pérez L, Piqueras J, Chioncel MF (2009) Magnetic transitions in α -
429 Fe₂O₃ nanowires. *J Appl Phys* 106:104302. doi: 10.1063/1.3259394
430
431 Eggleton RA, Fitzpatrick RW (1988) New data and a revised structural model for
432 ferrihydrite. *Clay Clay Miner* 36:111-124. doi: 10.1346/CCMN.1988.0360203
433
434 Fang XL, Chen C, Jin MS, Kuang Q, Xie ZX, Xie SY, Huang RB, Zheng LS (2009)
435 Single-crystal-like hematite colloidal nanocrystal clusters: synthesis and applications
436 in gas sensors, photocatalysis and water treatment. *J Mater Chem* 19:6154-6160. doi:
437 10.1039/b905034e
438
439 Farmer VC (1974) The Infrared Spectra of Minerals. Mineralogical Society of Great
440 Britain & Ireland. Mineralogical Society Monograph 4
441
442 Galwey AK, Brown ME (1999) Decomposition of carbonates. Thermal
443 decomposition of ionic solids. Elsevier B.V. Ed, In, pp 345–364
444
445 Gubin SP, Koksharov YA, Khomutov GB, Yurkov GY (2005) Magnetic
446 nanoparticles: preparation, structure and properties. *Russ Chem Rev* 74:489-520. doi:
447 10.1070/RC2005v074n06ABEH000897
448
449 Guo P, Wei Z, Wang B, Ding Y, Li H, Zhang G, Zhao XS (2011) Controlled
450 synthesis, magnetic and sensing properties of hematite nanorods and microcapsules.
451 *Colloid Surface A* 380:234-240. doi: 10.1016/j.colsurfa.2011.02.026
452

453 Islam MS, Kusumoto Y, Abdulla-Al-Mamun M (2012) Novel rose-type magnetic
454 (Fe_3O_4 , $\gamma\text{-Fe}_2\text{O}_3$ and $\alpha\text{-Fe}_2\text{O}_3$) nanoplates synthesized by simple hydrothermal
455 decomposition. *Mater Lett* 66:165-167. doi: 10.1016/j.matlet.2011.08.057
456
457 Jacob J, Khadar MA (2010) VSM and Mössbauer study of nanostructured hematite. *J*
458 *Magn Magn Mater* 322:614-621. doi: 10.1016/j.jmmm.2009.10.025
459
460 Jia X, Yang L, Song H, Su Y (2011) Facile synthesis and magnetic properties of cross
461 $\alpha\text{-Fe}_2\text{O}_3$ nanorods. *Micro Nano Lett* 6:806-808. doi: 10.1049/mnl.2011.0367
462
463 Jia XH, Song HJ (2012) Facile synthesis of monodispersed $\alpha\text{-Fe}_2\text{O}_3$ microspheres
464 through template-free hydrothermal route. *J Nanopart Res* 14:663. doi:
465 10.1007/s11051-011-0663-x
466
467 Kletetschka G, Wasilewski PJ (2002) Grain size limit for SD hematite. *Phys Earth*
468 *Planet In* 129:173-179. doi: 10.1016/S0031-9201(01)00271-0
469
470 Kumar P, Krishna MG, Bhattacharya AK (2009) Effect of microstructural evolution
471 on magnetic properties of Ni thin films. *Bulletin of Materials Science* 32: 263-270.
472 doi: 10.1007/s12034-009-0040-x
473
474 Kumar P (2010) Magnetic Behavior of Surface Nanostructured 50-nm Nickel Thin
475 Films. *Nanoscale research letters* 5:1596-1602. doi: 10.1007/s11671-010-9682-2
476
477 Li GS, Smith Jr RL, Inomata H, Arai K (2002) Preparation and magnetization of
478 hematite nanocrystals with amorphous iron oxide layers by hydrothermal conditions.
479 *Mater Res Bull* 37:949-955. doi: 10.1016/S0025-5408(02)00695-5
480
481 Li L, Chu Y, Liu Y (2007) Synthesis and characterization of ring-like $\alpha\text{-Fe}_2\text{O}_3$.
482 *Nanotechnology* 18:105603. doi: 10.1088/0957-4484/18/10/105603
483
484 Li Z, Lai X, Wang H, Mao D, Xing C, Wang D (2009) Direct hydrothermal synthesis
485 of single-crystalline hematite nanorods assisted by 1,2-propanediamine.
486 *Nanotechnology* 20:245603. doi: 10.1088/0957-4484/20/24/245603
487
488 Liu C, Ma J, Liu Y (2011) Formation mechanism and magnetic properties of three
489 different hematite nanostructures synthesized by one-step hydrothermal procedure.
490 *Sci China Chem* 54:1607-1614. doi: 10.1007/s11426-011-4392-x
491
492 Liu H, Li P, Lu B, Wei Y, Sun Y (2009) Transformation of ferrihydrite in the
493 presence or absence of trace Fe(II): The effect of preparation procedures of
494 ferrihydrite. *J Solid State Chem* 182:1767-1771. doi: 10.1016/j.jssc.2009.03.030
495
496 Liu Q, Barrón V, Torrent J, Eeckhout SG, Deng C (2008) Magnetism of intermediate
497 hydromaghemite in the transformation of 2-line ferrihydrite into hematite and its
498 paleoenvironmental implications. *J Geophys Res* 113:B01103. doi:
499 10.1029/2007JB005207
500
501 Liu Q, Barrón V, Torrent J, Qin H, Yu Y (2010) The magnetismo of micro-sized
502 hematite explained. *Phys Earth Planet In* 183:387-397. doi:

503 10.1016/j.pepi.2010.08.008
504
505 Lovesey SW, Rodríguez-Fernández A, Blanco JA (2011) Parity-odd multipoles,
506 magnetic charges, and chirality in hematite α -Fe₂O₃. *Phys Rev B* 83:054427. doi:
507 10.1103/PhysRevB.83.054427
508
509 Lu BL, Xu XY, Wu D, Sun YH (2008) Preparation and Characterization of Porous
510 α -Fe₂O₃ Nanodisks. *Chin J Inorg Chem* 24:1690-1694.
511
512 Michel FM, Barrón V, Torrent J, Morales MP, Serna CJ, Boily JF, Liu Q, Ambrosini
513 A, Cismasu AC, Brown Jr GE (2010) Ordered ferrimagnetic form of ferrihydrite
514 reveals links among structure, composition, and magnetism. *P Natl Acad Sci USA*
515 107:2787-2792. doi: 10.1073/pnas.0910170107
516
517 Mitra S, Das S, Mandal K, Chaudhuri S (2007) Synthesis of a α -Fe₂O₃ nanocrystals in
518 its different morphological attributes: grow mechanism, optical and magnetic
519 properties. *Nanotechnology* 18:275608. doi: 10.1088/0957-4484/18/27/275608
520
521 Muruganandham M, Amutha R, Sathish M, Singh TS, Suri RPS, Sillanpää MJ (2011)
522 Facile Fabrication of Hierarchical α -Fe₂O₃: Self-Assembly and Its Magnetic and
523 Electrochemical Properties. *Phys Chem C* 115:18164-18173. doi: 10.1021/jp205834m
524
525 Ni H, Ni Y, Zhou Y, Hong J (2012) Microwave-hydrothermal synthesis,
526 characterization and properties of rice-like α -Fe₂O₃ nanorods. *Mater Lett* 73:206-208.
527 doi: 10.1016/j.matlet.2012.01.065
528
529 Ni S, Lin S, Pan Q, Yang F, Huang K, Wang X, He D (2009) Synthesis of core-shell
530 α -Fe₂O₃ hollow micro-spheres by a simple two-step process. *J Alloy Compd* 478:876-
531 879. doi: 10.1016/j.jallcom.2008.12.038
532
533 Pan Q, Huang K, Ni S, Yang F, Lin S, He D (2009) Synthesis of α -Fe₂O₃ dendrites by
534 a hydrothermal approach and their application in lithium-ion batteries. *J Phys D Appl*
535 *Phys* 42:015417. doi: 10.1088/0022-3727/42/1/015417
536
537 Peng D, Beysen S, Li Q, Sun Y, Yang L (2010) Hydrothermal synthesis of
538 monodisperse α -Fe₂O₃ hexagonal platelets. *Particuology* 8:386-389. doi:
539 10.1016/j.partic.2010.05.003
540
541 Raiswell R, Vu HP, Brinza L, Benning LG (2010) The determination of Fe in
542 ferrihydrite by ascorbic acid extraction: methodology, dissolution kinetics and loss of
543 solubility with age and de-watering. *Chem Geol* 278:70-79. doi:
544 10.1016/j.chemgeo.2010.09.002
545
546 Rath C, Sahu KK, Kulkarni SD, Anand S, Date SK, Das RP, Mishra NC (1999)
547 Microstructure-dependent coercivity in monodispersed hematite particles. *Appl Phys*
548 *Lett* 75:4171-4173. doi: 10.1063/1.125572
549
550 Rodriguez-Blanco JD, Shaw S, Benning LG (2008) How to make 'stable' ACC:
551 protocol and preliminary structural characterization. *Mineral Mag* 72:283-286. doi:
552 10.1180/minmag.2008.072.1.283

553
554 Roncal-Herrero T, Rodriguez-Blanco JD, Benning LG, Oelkers EH (2009)
555 Precipitation of iron and aluminum phosphates directly from aqueous solution as a
556 function of temperature from 50 to 200 °C. *Cryst Growth Des* 9:5197-5205. doi:
557 10.1021/cg900654m
558
559 Rout K, Mohapatra M, Anand S (2012) 2-Line ferrihydrite: synthesis, characterization
560 and its adsorption behavior for removal of Pb(II), Cd(II), Cu(II) and Zn(II) from
561 aqueous solutions. *Dalton Trans* 41:3302-3312. doi: 10.1039/c2dt11651k
562
563 Sahu KK, Rath C, Mishra NC, Anand S, Das RP (1997) Microstructural and magnetic
564 Studies on hydrothermally prepared hematite. *J Colloid Interf Sci* 185:402-410. doi:
565 10.1006/jcis.1996.4525
566
567 Scherrer P (1918) Estimation of the size and internal structure of colloidal particles by
568 means of röntgen. *Nachr Ges Wiss Göttingen Math-Pys Kl* 2:96-100.
569
570 Schneeweiss O, Grygar T, David B, Zboril R, Filip J, Mashlan M (2008) Mössbauer
571 and magnetic studies of nanocrystalline iron, iron oxide and iron carbide powders
572 prepared from synthetic ferrihydrite. *Aip Conf Proc* 1070:106-113. doi:
573 10.1063/1.3030834
574
575 Schwertmann U, Taylor RM (1972) The transformation of lepidocrocite to goethite.
576 *Clay Clay Miner* 20:151-158. doi: 10.1346/CCMN.1972.0200306
577
578 Song F, Guan J, Fan X, Yan G (2009) Single-crystal star-like arrayed particles of
579 hematite: Synthesis, formation mechanism and magnetic properties. *J Alloy Compd*
580 485:753-758. doi: 10.1016/j.jallcom.2009.06.075
581
582 Song HJ, Li N, Shen XQ (2011) Template-free synthesis of hollow α -Fe₂O₃
583 microspheres. *Appl Phys A-Mater* 102:559-563. doi: 10.1007/s00339-010-6072-7
584
585 Sreeram KJ, Nidhin M, Nair BU (2009) Synthesis of aligned hematite nanoparticles
586 on chitosan-alginate films. *Colloid Surface B* 71:260-267. doi:
587 10.1016/j.colsurfb.2009.02.015
588
589 Stanjek H, Weidler PG (1992) The effect of dry heating on the chemistry, surface
590 area, and oxalate solubility of synthetic 2-line and 6-line ferrihydrites. *Clay Miner*
591 27:397-412. doi: 10.1180/claymin.1992.027.4.01
592
593 Suber L, Imperatori P, Mari A, Marchegiani G, Mansilla MV, Fiorani D, Plunkett
594 WR, Rinaldi D, Cannas C, Ennas G, Peddis D (2010) Thermal hysteresis of Morin
595 transition in hematite particles. *Phys Chem Chem Phys* 12:6984-6989. doi:
596 10.1039/b925371h
597
598 Suresh R, Vijayaraj A, Giribabu K, Manigandan R, Prabu R, Stephen A, Thirumal E,
599 Narayanan V (2013) Fabrication of iron oxide nanoparticles: magnetic and
600 electrochemical sensing property. *J Mater Sci-Mater El* 24:1256-1263. doi:
601 10.1007/s10854-012-0916-1
602

603 Tadic M, Citakovic N, Panjan M, Stanojevic B, Markovic D, Jovanovic D, Spasojevic
604 V (2012) Syntesis, morphology, microstructure and magnetic properties of hematite
605 submicron particles. *J Alloy Compd* 543:118-124. doi: 10.1016/j.jallcom.2012.07.047
606

607 Tadić M, Čitaković N, Panjan M, Stojanović Z, Marković D, Spasojević V (2011)
608 Synthesis, morphology, microstructure and magnetic properties of hematite
609 submicron particles. *J Alloy Compd* 509:7639-7644. doi:
610 10.1016/j.jallcom.2011.04.117
611

612 Tsuzuki T, Schäffel F, Muroi M, McCormick PG (2011) α -Fe₂O₃ nano-platelets
613 prepared by mechanochemical/termal processing. *Powder Technol* 210:198-202. doi:
614 10.1016/j.powtec.2011.03.012
615

616 Vallina B, Rodriguez-Blanco JD, Brown AP, Blanco JA, Benning LG (2013)
617 Amorphous dysprosium carbonate: characterization, stability, and crystallization
618 pathways. *J Nanopart Res* 15:1438. doi: 10.1007/s11051-013-1438-3
619

620 Vu HP, Shaw S, Brinza L, Benning LG (2010) Crystallization of hematite (α -Fe₂O₃)
621 under alkaline condition: the effects of Pb. *Cryst Growth Des* 10:1544-1551. DOI.
622 doi: 10.1021/cg900782g
623

624 Wang H, Geng WC, Wang Y (2011) Preparation of nanoparticles and hollow spheres
625 of alpha-Fe₂O₃ and their properties. *Res Chem Intermediat* 37:389-395. doi:
626 10.1007/s11164-011-0269-z
627

628 Xia C, Hu C, Xiong Y, Wang N (2009) Synthesis of α -Fe₂O₃ hexagons and their
629 magnetic properties. *J Alloy Compd* 480:970-973. doi: 10.1016/j.jallcom.2009.02.106
630

631 Xu JS, Zhu YJ (2012) α -Fe₂O₃ hierarchically nanostructured mesoporous
632 microspheres: Surfactant-free solvothermal combined with heat treatment synthesis,
633 photocatalytic activity and magnetic property. *Crystengcomm* 14:2702-2710. doi:
634 10.1039/C2CE06473A
635

636 Xu JS, Zhu YL, Chen F (2013) Solvothermal synthesis, characterization and magnetic
637 properties of α -Fe₂O₃ and Fe₃O₄ flower-like hollow microspheres. *J Solid State Chem*
638 199:204-211. doi: 10.1016/j.jssc.2012.12.027
639

640 Xu W, Hausner DB, Harrington R, Lee PL, Strongin DR, Parise JB (2011) Structural
641 water in ferrihydrite and constraints this provides on possible structure models. *Am*
642 *Mineral* 96:513-520. doi: 10.2138/am.2011.3460
643

644 Xu YY, Rui XF, Fu YY, Zhang H (2005) Magnetic properties of α -Fe₂O₃ nanowires.
645 *Chem Phys Lett* 410:36-38. doi: 10.1016/j.cplett.2005.04.090
646

647 Xu YY, Zhao D, Zhang XJ, Jin WT, Kashkarov P, Zhang H (2009) Synthesis and
648 characterization of single-crystalline α -Fe₂O₃ nanoleaves. *Physica E* 41:806-811. doi:
649 10.1016/j.physe.2008.12.015
650

651 Yadav LDS (2005) Organic Spectroscopy. Anamaya Publishers, New Delhi.
652

653 Yang Y, Yi JB, Huang XL, Xue JM, Ding J. (2011) High-coercivity in α -Fe₂O₃
654 formed after annealing from Fe₃O₄ formed nanoparticles. IEEE T Magn 47:3340-
655 3342. doi: 10.1109/TMAG.2011.2159487
656
657 Yao R, Cao C (2012) Self-assembly of α -Fe₂O₃ mesocrystals with high coercivity.
658 RSC Adv 2:1979-1985. doi: 10.1039/c2ra00796g
659
660 Yu JY, Park M, Kim J (2002) Solubilities of synthetic schwertmannite and
661 ferrihydrite. Geochim J 36:119-132.
662
663 Zeng S, Tang K, Li T (2007) Controlled synthesis of α -Fe₂O₃ nanorods and its size-
664 dependent optical absorption, electrochemical, and magnetic properties. J Colloid
665 Interf Sci 312:513-521. doi: 10.1016/j.jcis.2007.03.046
666
667 Zhang XH, Chen YZ, Liu H, Wei Y, Wei W (2013) Controllable synthesis, formation
668 mechanism and magnetic properties of hierarchical alpha-Fe₂O₃ with various
669 morphologies. J Alloy Compd 55:74-81. doi: 10.1016/j.jallcom.2012.12.025
670
671 Zhang YC, Tang JY, Hu XY (2008) Controllable synthesis and magnetic properties
672 of pure hematite and maghemite nanocrystals from a molecular precursor. J Alloy
673 Compd 462:24-28. doi: 10.1016/j.jallcom.2007.07.115
674
675 Zhang ZJ, Chen XY (2009) Magnetic greigite (Fe₃S₄) nanomaterials: Shape-
676 controlled solvothermal synthesis and their calcination conversion into hematite (α -
677 Fe₂O₃) nanomaterials. J Alloy Compd 488:339-345. doi:
678 10.1016/j.jallcom.2009.08.127
679
680 Zhao J, Huggins FE, Feng Z, Huffman GP (1994) Ferrihydrite: Surface structure and
681 its effects on phase transformation. Clay Clay Miner 42:737-746.
682
683 Zhong SL, Song JM, Zhang S, Yao H, Xu AW, Yao WT, Yu SH (2008) Template-
684 free hydrothermal synthesis and formation mechanism of hematite microrings. J Phys
685 Chem C 112:19916-19921. doi: 10.1021/jp806665b
686
687 Zhu LP, Xiao HM, Liu XM, Fu SY (2006) Template-free synthesis and
688 characterization of novel 3D urchin-like α -Fe₂O₃ superstructures. J Mater Chem
689 16:1794-1797. doi: 10.1039/b604378j
690
691 Zhu W, Cui X, Wang L, Liu T, Zhang Q (2011) Monodisperse porous pod-like
692 hematite: hydrothermal formation, optical absorbance, and magnetic properties. Mater
693 Lett 65:1003-1006. doi: 10.1016/j.matlet.2010.12.053
694
695 Zysler RD, Vasquez-Mansilla M, Arciprete C, Dimitrijewits M, Rodriguez-Sierra D,
696 Saragovi C (2001) Structure and magnetic properties of thermally treated
697 Nanoematite. J Magn Magn Mater 224:39-48. doi: 10.1016/S0304-8853(00)01365-2
698
699 Zysler RD, Vasquez-Mansilla M, Fiorani D (2004) Surface effects in α -Fe₂O₃
700 nanoparticles. Eur Phys J B 41:171-175. doi: 10.1140/epjb/e2004-00306-7
701
702

703
704
705
706

707 **FIGURE CAPTIONS**

708

709 **Fig. 1** TEM images of carbonated 2-line ferrihydrite. The top and bottom insets show
710 the EDX spectrum (Cu signal comes from the Cu support grid) and SAED pattern
711 obtained from the sample

712

713 **Fig. 2** Powder X-ray diffraction pattern of the carbonated 2-line ferrihydrite. Inset:
714 FTIR spectrum of carbonated 2-line ferrihydrite precursor. The band assignments are
715 detailed in Table 1

716

717 **Fig. 3** TGA (sample weight loss and weight loss rate curves) of carbonated 2-line
718 ferrihydrite

719

720 **Fig. 4** 3D X-ray diffraction plot showing the transformation of carbonated 2-line
721 ferrihydrite to α -Fe₂O₃ with increasing annealing temperature

722

723 **Fig. 5** Pattern-matching refinements of the powder X-ray diffraction patterns of α -
724 Fe₂O₃ after the dry heat treatment at 350, 600, 800 and 1000 °C. Points correspond to
725 the experimental data; the solid lines are the calculated profiles. Tick marks below the
726 patterns represent the positions of allowed reflections. The difference curves are
727 plotted at the bottom of the patterns showing the difference between the experimental
728 and calculated profiles

729

730 **Fig. 6** Secondary electron FEG-SEM images of the α -Fe₂O₃ samples produced at 350
731 (a), 600 (b), 800 (c) and 1000 °C (d)

732

733 **Fig. 7** HR-TEM microphotographs and corresponding SAED patterns of α -Fe₂O₃
734 samples produced at 350 (a, b), 600 (c, d), 800 (e, f), and 1000 °C (g, h). α -Fe₂O₃
735 nanoparticles with a subparticle structure with sizes down to ~20 nm (i, j)

736

737 **Fig. 8** Hysteresis loops of the α -Fe₂O₃ nanoparticles obtained at 350 (a), 600 (b), 800
738 (c) and 1000 °C (d)

739

740 **Fig. 9** Variation of coercivity with particle size and Scherrer crystallite size.
741 Horizontal error bars in particle size data correspond to the standard deviation of 100
742 measurements. Vertical error bars correspond to the standard deviation of four
743 coercivity measurements. Inset shows the variation of the coercivity and
744 magnetization energy density with temperature.
745
746

747 **TABLES**

748

749 **Table 1** FTIR stretching (ν) and bending (δ) vibrational bands for carbonated 2-
750 line ferrihydrite

751

Band number	Wavelength (cm ⁻¹)*	Mode of vibration	Bibliography
1	3700-2300	ν (O-H)	Liu et al. 2009; Farmer 1974
2	2463-2332	ν CO ₂	Yadav 2005
3	1633	δ (O-H)	Farmer 1974
4	1455	ν_3 asym. CO ₃	Liu et al. 2009; Andersen and Brečević 1991
5	1385	Fe-OH	Rout et al. 2012
6	1338	Fe-OH	Rout et al. 2012
7	1042	ν_1 CO ₃	Andersen 1991
8	824	δ (Fe-OH)	Rout et al. 2012

752

753

754

755

756 **Table 2** Microstructural-dependent magnetic properties of α -Fe₂O₃ nanoparticles
757 obtained from carbonated 2-line ferrihydrite. Hc is the magnetic coercive field, while
758 Mr is the remanent magnetization

Temp. (° C)	Heating time (h)	Morphology	Size (nm) ⁽¹⁾ L (length), W (width)	Scherrer crystallite size (nm)	Hc (Oe) ⁽²⁾	Mr (emu/g)
350	8	Pseudospheric	L=20±6, W=15±4	20(1)	289±29	0.007(1)
600	13	Pseudospheric	L=71±19, W=52±16	55(3)	1720±207	0.033(5)
800	16	Prismatic	L=202±101, W=136±46	92(4)	3837±123	0.011(4)
1000	20	Prismatic	L=352±109, W=277±103	131(6)	5027±46	0.025(5)

759

760 (1) Values correspond to the average and standard deviation of 100 nanoparticles.

761 (2) Values correspond to the average and standard deviation of 4 magnetic coercivity measurements.

762

763

764

765

766

767

Figure 1
[Click here to download high resolution image](#)

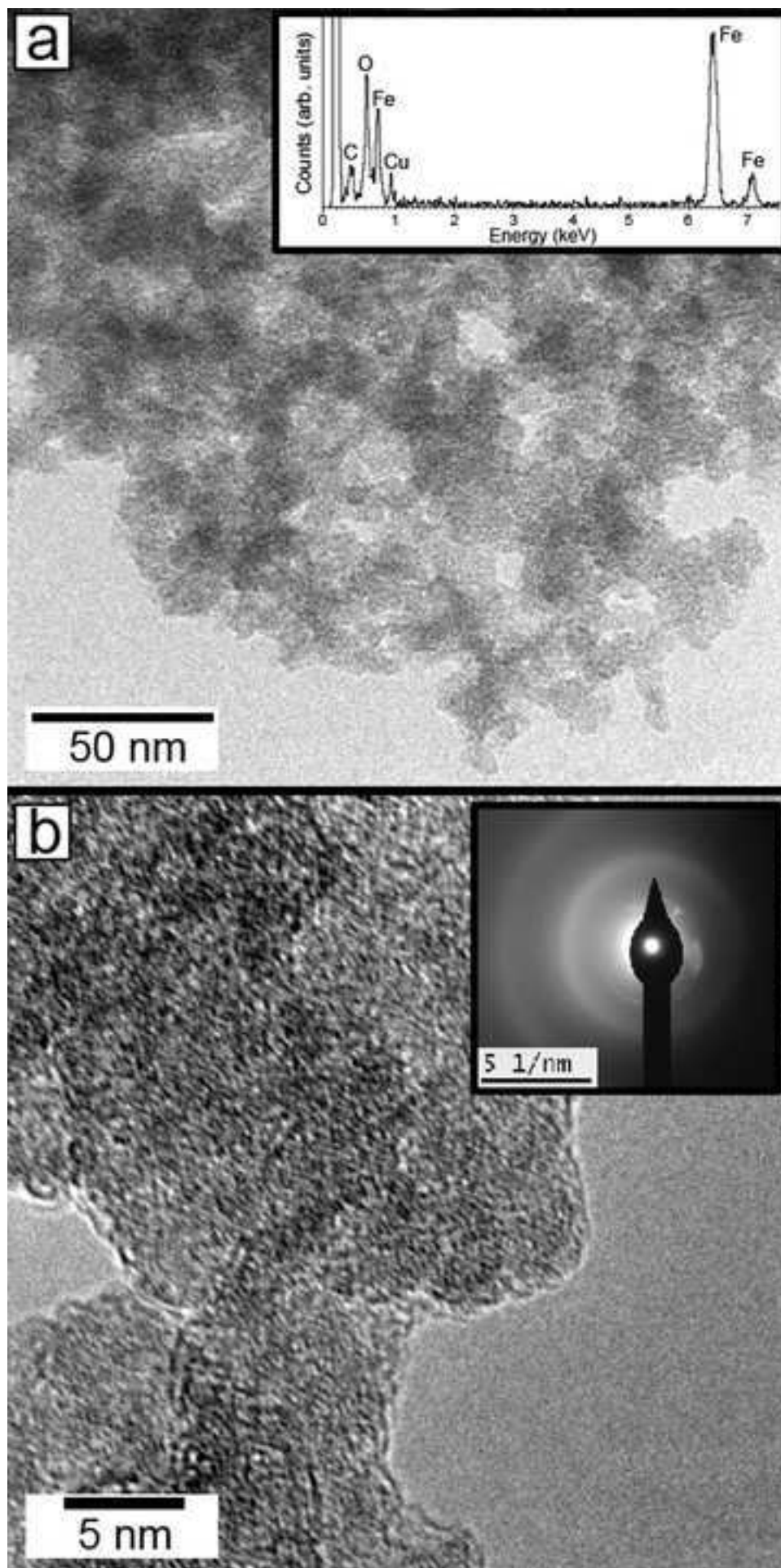


Figure 2
[Click here to download high resolution image](#)

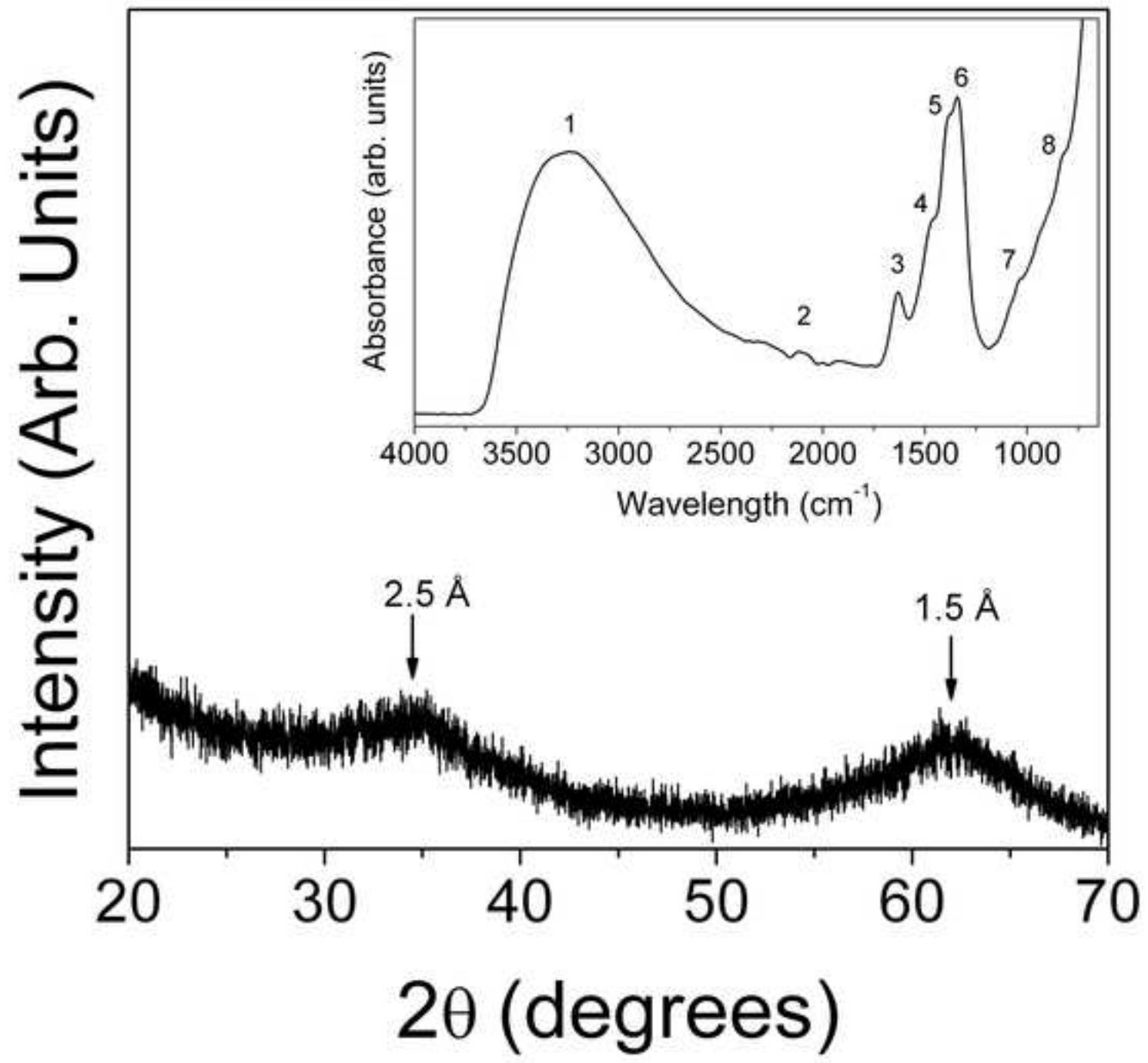


Figure 3
[Click here to download high resolution image](#)

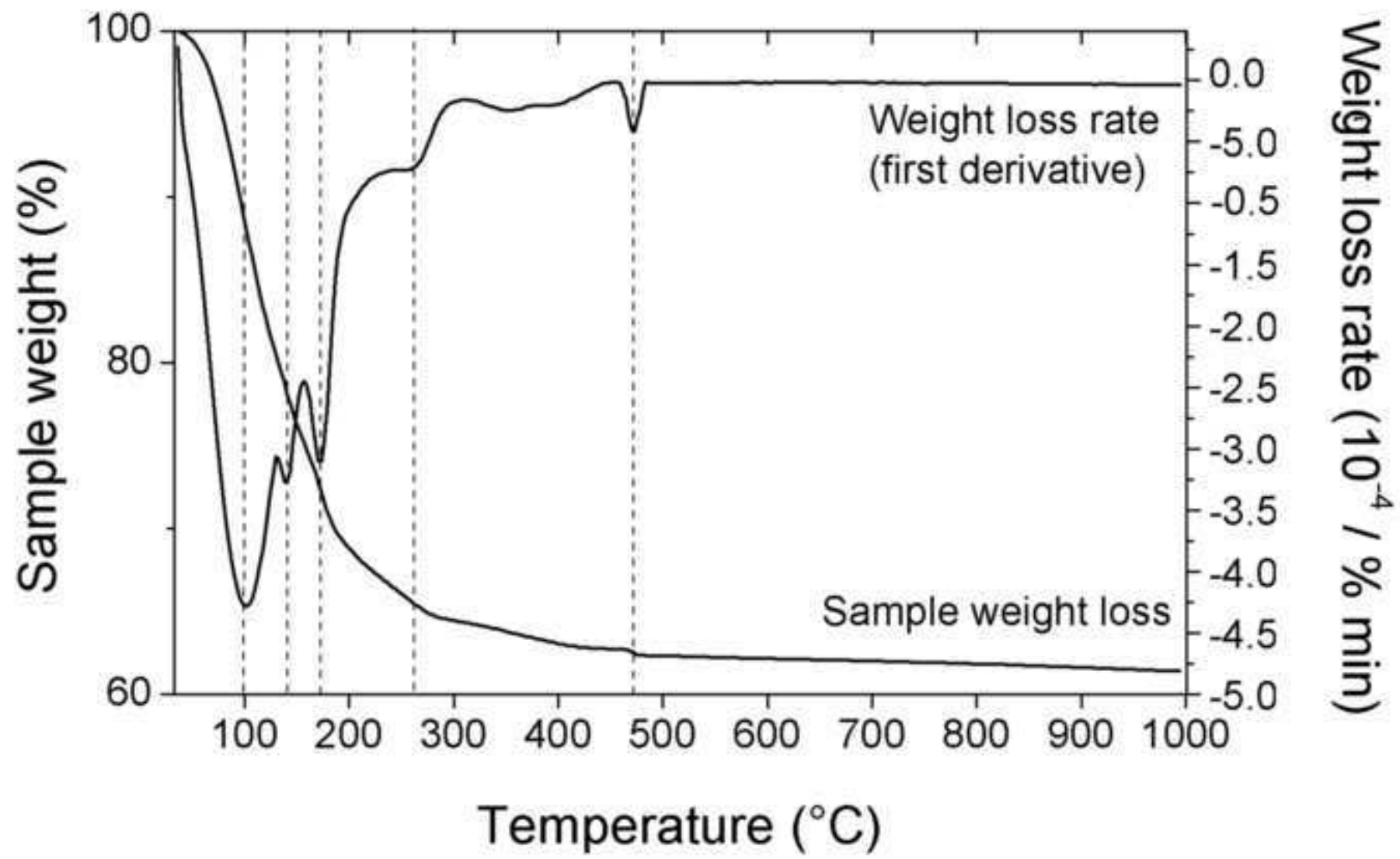


Figure 4
[Click here to download high resolution image](#)

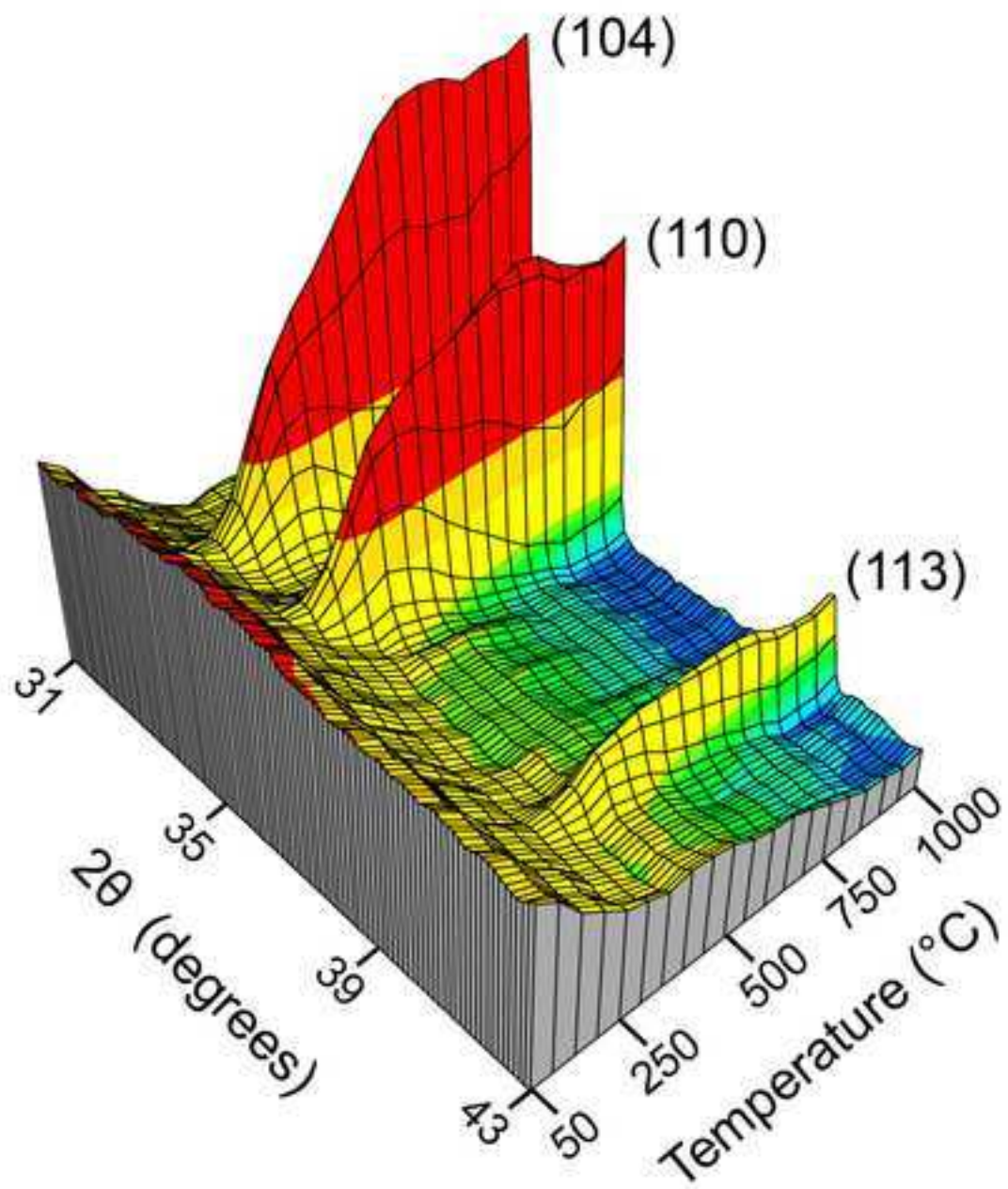


Figure 5
[Click here to download high resolution image](#)

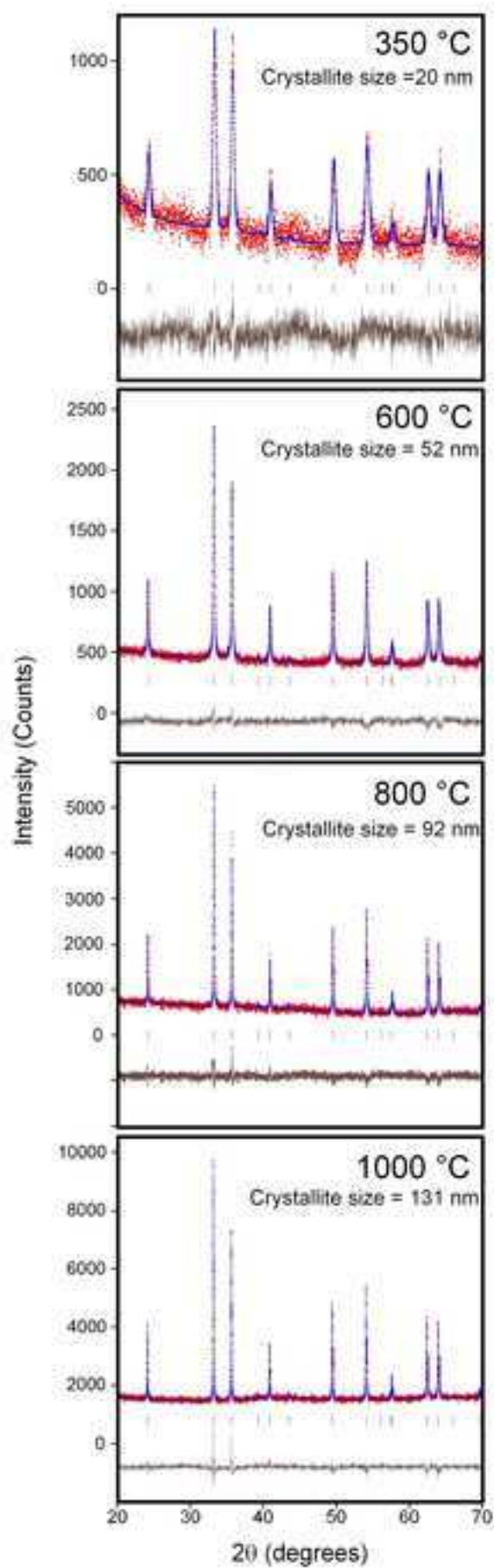


Figure 6
[Click here to download high resolution image](#)

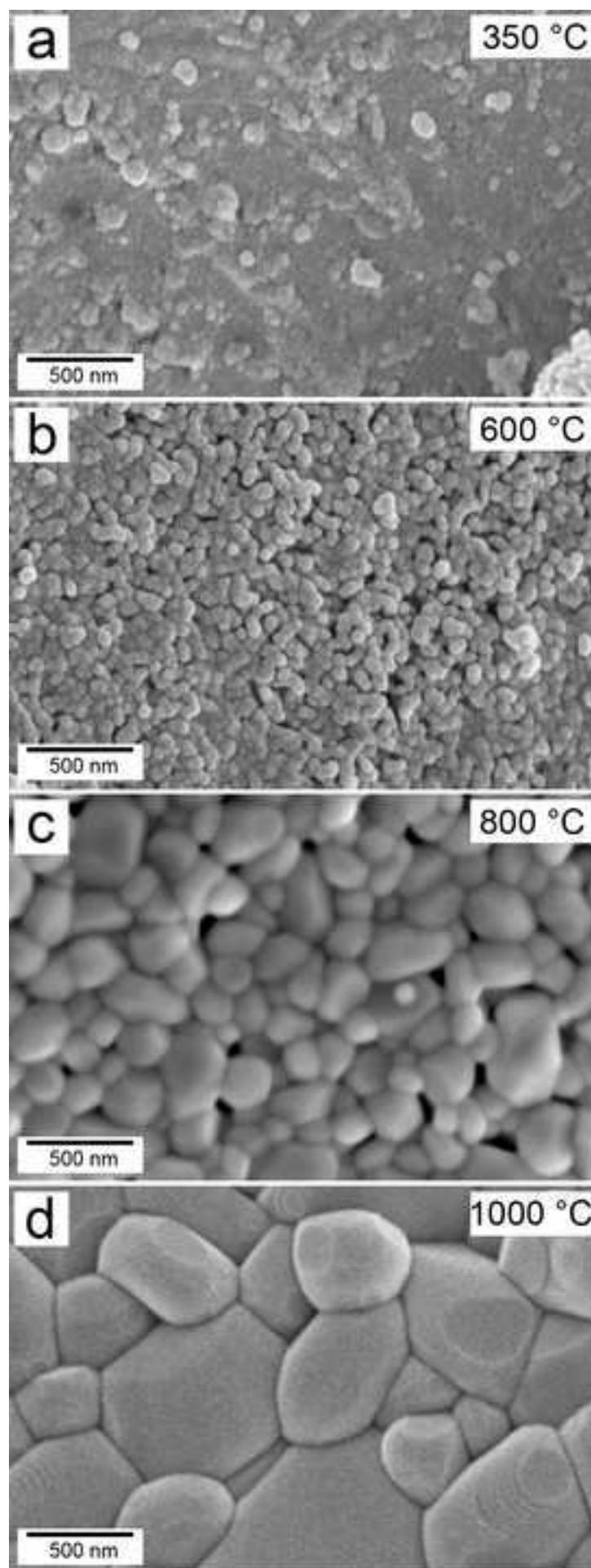


Figure 7

[Click here to download high resolution image](#)

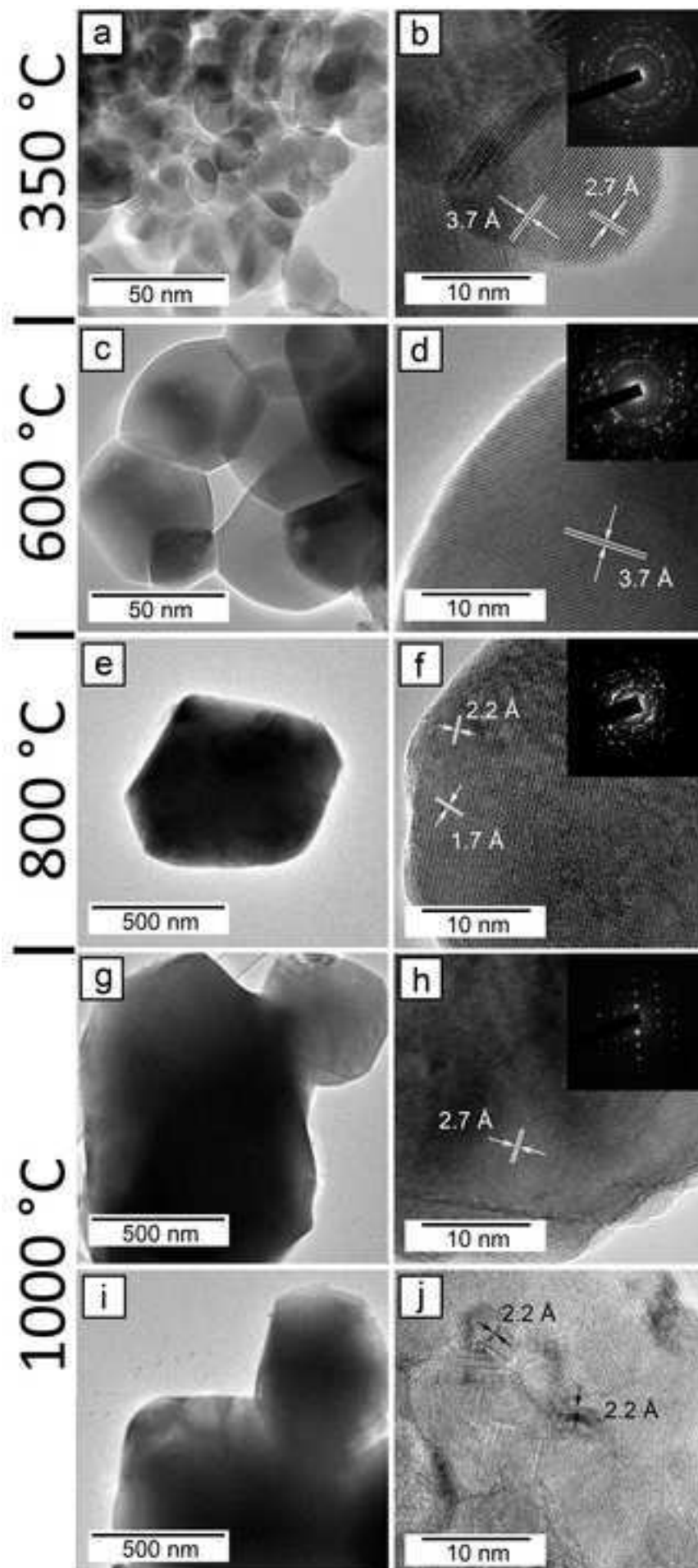


Figure 8

[Click here to download high resolution image](#)

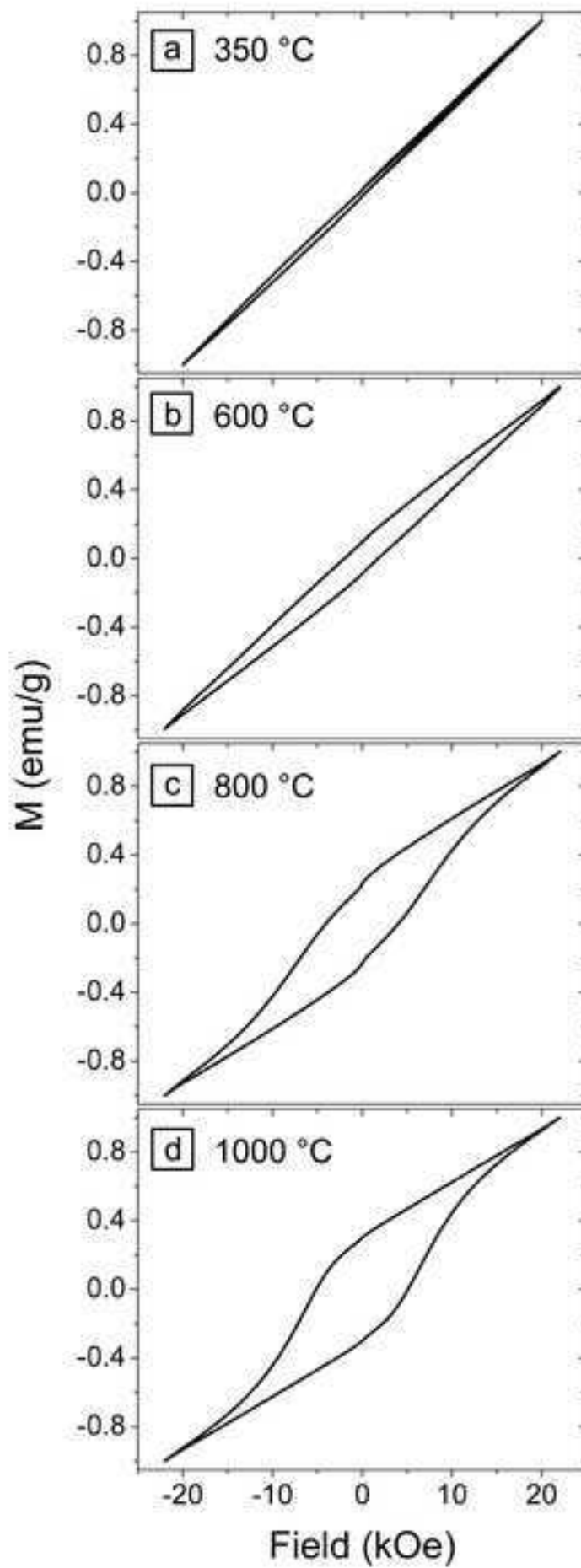
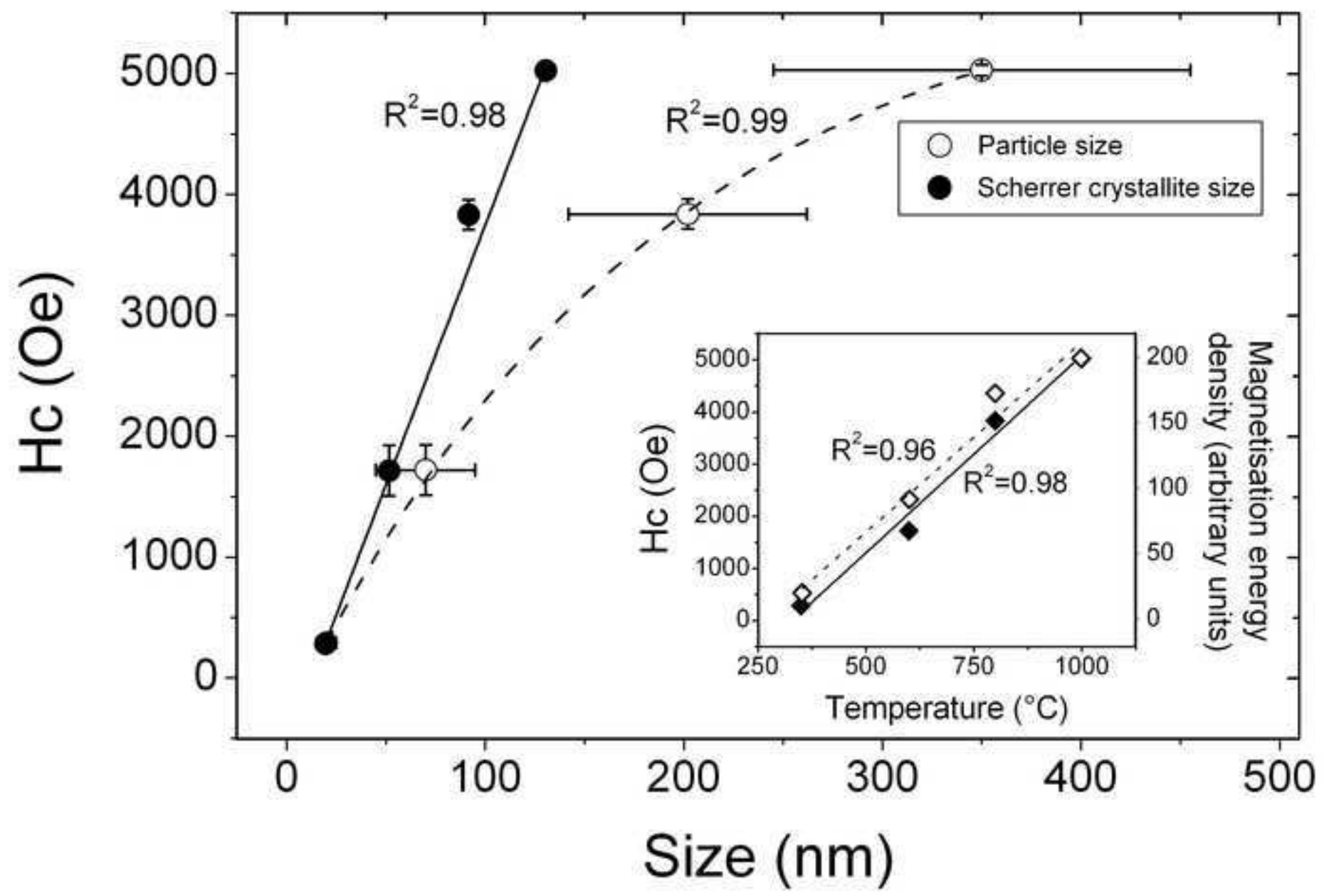


Figure 9
[Click here to download high resolution image](#)



Revised supplementary information

[Click here to download Supplementary material \(audio/video files etc\): Vallina et al JNR - SUPPLEMENTARY INFORMATION.pdf](#)